2025 IEEE/SICE International Symposium on System Integration (SII)
January 21-24, 2025, Munich, Germany

Development of chiseling model with transition from chiseling to splitting situations for implementing to surgical training simulator*

Shota Kasai[1], Sinyoung Lee[2], and Yoshiyuki Noda[1]

Abstract— **This paper contributes to realize the surgical training simulator for the chiseling operation to a hard tissue using a bone chisel and mallet. In most of the previous studies related to the training simulator, the target organization was soft tissues. However, in oral and orthopedics surgeries, surgeons operate hard tissues such as bone and teeth using a chisel and mallet. Therefore, the development of the surgical training simulator for chiseling the hard tissue by pounding the bone chisel with bone mallet has been promoted in recent year. It is required to represent precisely the chiseling situation for improving the realistic sensation. In this study, we propose the chiseling model with the transition from chiseling to splitting in response to pound the chisel. In the proposed model, the mass, spring and damper model with varying the equilibrium point is applied for representing the elastic and plastic deformation of hard tissue. Moreover, the model parameters are switched for representing the transition from chiseling to splitting. The model parameters are identified by fitting the simulated and the experimented chiseling data. In this study, the measurement of the chiseling motion is also introduced for actual chiseling data acquisition. The efficacy of the proposed model is verified by the comparison with the experimental results from measurement system.**

I. INTRODUCTION

In recent years, various surgical training simulators have been developed with the progress of medical technologies[1][2]. These simulators can enhance the sense of immersion and reality using around view monitors or a head mount display and reaction force display using haptic device. The surgical training simulators have also been used for planning preliminary the operation[3]. The surgical accidents can be reduced by planning with the simulator creating the high realistic sensation. In these force display devices, high responsiveness of the manipulated parts is required for creating the touching sensation to objects. The high responsiveness can be realized by lightening the manipulated parts. Most conventional surgical training simulators have been designed for soft tissues and rotary instruments such as drills[4][5]. Simulators and mathematical model to represent the sensation of the surgery have also been developed for surgeries performed with saws, which are used for hard tissues such as bones and teeth[6][7]. However, in orthopedic and oral surgeries, the surgeons operate hard tissue using a chisel and a mallet. The conventional surgical training simulators whose manipulated parts are light weight can be broken by the large impact forces such as pounding chisel.

Therefore in our previous studies[8][9], we developed the surgical training simulator for simulating virtually the chisel operation. This simulator has the force display device with arranging orthogonally linear guides to achieve high stiffness and implementing two-degree-of-freedom admittance control method to react instantaneously to the impact forces.

In these previous studies, the movement sensation of chisel in the air, the contacting sensation to the hard tissue, the stabbing sensation to the hard tissue and the pulling sensation from the hard tissue were created by implementing these virtual models to the admittance control system. However, the virtual models have not been evaluated by comparing to the actual motions. It is required to evaluate the virtual model to the chiseling and splitting motions as basic motions of the chiseling operation. In this study, we develop the virtual model to the chiseling and splitting motion and the model parameters are identified by comparing to the actual chiseling motion. The measurement system of chiseling motion has been proposed in our previous study[10]. In this study, we introduce the measurement system of chiseling motion for comparing between the simulated and the actual motions. In the measurement system, an Inertial Measurement Unit Sensor (IMU sensor) is attached to the chisel in order to estimate its posture. In addition, the movement of the chisel is detected by a Light Detection and Ranging (LiDAR) camera, and the displacement of the chisel is estimated by the sensor fusion in which the data of IMU sensor and LiDAR camera is integrated. The impact force applied to the chisel is measured by a 6-axis force sensor. Based on these measured and estimated data, the chiseling and splitting motion are represented by a mechanical model. In this study, the elastic and plastic deformation due to the chiseling and splitting can be represented by the spring-mass-damper model with equilibrium point. The splitting sensation can be created by the virtual model in which the model parameters according to the motion of equilibrium point are switched from the chiseling model. In this study, in order to obtain basic data with high reproducibility, we performed chiseling operations on Acrylonitrile Butadiene Styrene resin (ABS resin). And we verified the effectiveness of the proposed chiseling and splitting model by comparing it with experimental measurements.

II. MEASUREMENT SYSTEM

The measurement system of chiseling motion in this study is shown in Fig. 1(a). The chisel has the IMU sensor, TDK

*This work was not supported by any organization

[1]S. Kasai and Y. Noda are with the Department of Mechanical Engineering, University of Yamanashi, 4-3-11, Takeda, Kofu, Yamanashi, 400-8511, Japan. g23tm005@yamanashi.ac.jp, noday@yamanashi.ac.jp

[2]S. Lee is with the Graduate School of Engineering Science, Osaka University, 1-3 Machikaneyama, Toyonaka, Osaka, 560-8531, Japan. sylee@bpe.es.osaka-u.ac.jp

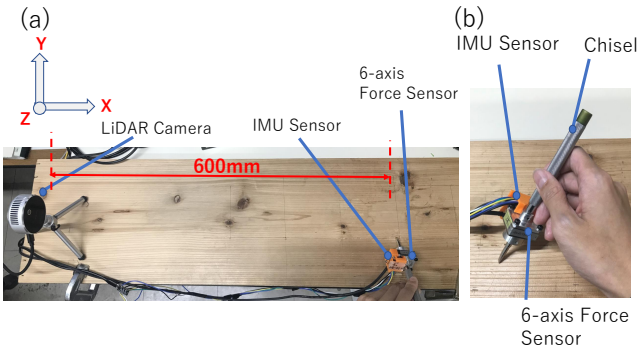

Fig. 1. Overall view of measurement device for chiseling. (a) Overview system; (b) Sensors placement with chisel.

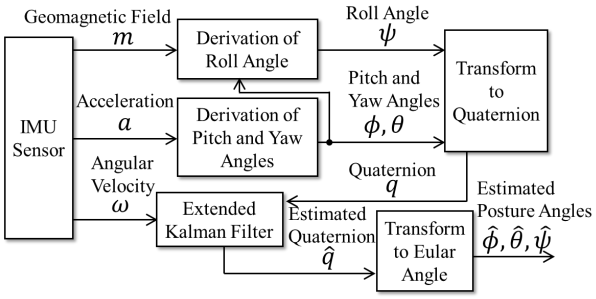

Fig. 2. Signal flow diagram of chisel's posture angles estimation.

InvenSense ICM-20948 to measure the posture of the chisel and six-axis force sensor, Leptrino SFS0122 to measure the impact force applied by operator. In addition, the LiDAR camera, Intel Realsense L515, is located 600 mm away from the chiseling.

A. Measurement posture angles of chisel

The posture angles of the chisel are estimated by the IMU sensor using sensor fusion technology. The signal flow diagram of the sensor fusion is shown in Fig. 2. The relation between the sensor coordinate and inertial coordinate is shown in Fig. 3. As shown in Fig. 3, the Z axis of inertial coordinate system is defined vertically upward, the X axis in the inertial coordinates aligned along a geomagnetic field, and the rotation order of the Euler angles is defined as z-y-x. The pitch, the yaw, the roll angles of the chisel are shown as ϕ, θ, ψ, respectively.

The pitch angle ϕ, and the yaw angle θ can be estimated from the gravitational acceleration as

$$\phi = \tan^{-1}\frac{a_y}{a_z}, \tag{1}$$

$$\theta = \tan^{-1}\frac{-a_x}{\sqrt{a_y^2 + a_z^2}}, \tag{2}$$

where a_x, a_y, a_z are the acceleration detected by the IMU sensor. The roll angle ψ can be estimated using the pitch

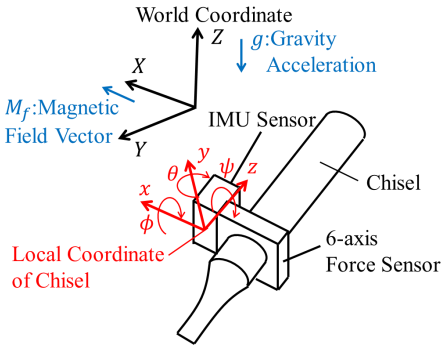

Fig. 3. Coordinate system in chiseling motion.

angle ϕ, yaw angle θ as

$$\begin{bmatrix} M_X \\ M_Y \end{bmatrix} = \begin{bmatrix} \cos\theta & -\sin\phi\sin\theta & -\cos\phi\sin\theta \\ 0 & \cos\phi & -\sin\phi \end{bmatrix} \begin{bmatrix} m_x \\ m_y \\ m_z \end{bmatrix}, \tag{3}$$

$$\psi = \tan^{-1}\frac{-M_Y}{M_X}, \tag{4}$$

where m_x, m_y, m_z are the geomagnetic field on the sensor coordinate detected by the IMU sensor. M_X and M_Y are the geomagnetic field on the inertial coordinate without the z-axis rotation.

This study used quaternions in order to estimate posture angles of the chisel to prevent gimbal lock. The Euler angle u can be transformed to the quaternion q as

$$q = t_{qe}, \tag{5}$$

$$q = \begin{bmatrix} q_0 & q_1 & q_2 & q_3 \end{bmatrix}^T, \tag{6}$$

$$u = \begin{bmatrix} \phi & \theta & \psi \end{bmatrix}^T, \tag{7}$$

$$t_{qe}(u) = \begin{bmatrix} \cos(\frac{\phi}{2})\cos(\frac{\theta}{2})\cos(\frac{\psi}{2}) + \sin(\frac{\phi}{2})\sin(\frac{\theta}{2})\sin(\frac{\psi}{2}) \\ \sin(\frac{\phi}{2})\cos(\frac{\theta}{2})\cos(\frac{\psi}{2}) - \cos(\frac{\phi}{2})\sin(\frac{\theta}{2})\sin(\frac{\psi}{2}) \\ \cos(\frac{\phi}{2})\sin(\frac{\theta}{2})\cos(\frac{\psi}{2}) + \sin(\frac{\phi}{2})\cos(\frac{\theta}{2})\sin(\frac{\psi}{2}) \\ \cos(\frac{\phi}{2})\cos(\frac{\theta}{2})\sin(\frac{\psi}{2}) - \sin(\frac{\phi}{2})\sin(\frac{\theta}{2})\cos(\frac{\psi}{2}) \end{bmatrix}. \tag{8}$$

The outputs are converted from quaternions to Euler angles. The transform can be performed as

$$u = t_{eq}(q), \tag{9}$$

$$t_{eq}(q) = \begin{bmatrix} \tan^{-1}(\frac{c_{23}}{c_{33}}) & \sin^{-1}(-\frac{c_{13}}{\sqrt{c_{23}^2 + c_{33}^2}}) & \tan^{-1}(\frac{c_{12}}{c_{11}}) \end{bmatrix}^T, \tag{10}$$

$$C = \begin{bmatrix} q_1^2 - q_2^2 - q_3^2 + q_0^2 & 2(q_1q_2 + q_3q_0) & 2(q_3q_1 - q_2q_0) \\ 2(q_1q_2 - q_3q_0) & q_2^2 - q_3^2 - q_1^2 + q_0^2 & 2(q_2q_3 + q_1q_0) \\ 2(q_3q_1 + q_2q_0) & 2(q_2q_3 - q_1q_0) & q_3^2 - q_1^2 - q_2^2 + q_0^2 \end{bmatrix}, \tag{11}$$

where C is the direction cosine matrix, and the indices i and j in C_{ij} represent the numbers of the matrix elements. And the relation between the quaternion q and the angular velocity

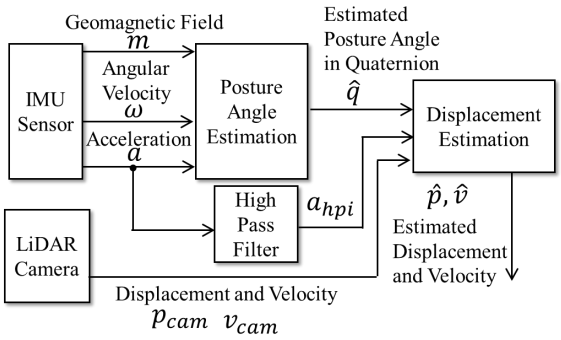

Fig. 4. Signal flow diagram of chisel's displacement and velocity estimation by sensor fusion technology.

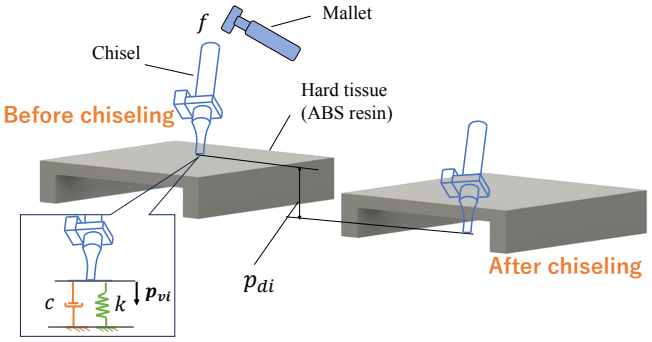

Fig. 5. Dynamics of virtual chiseling and splitting model.

w can be represented from (5) as

$$\dot{q} = \frac{dt_{qe}(u)}{dt} = \frac{\partial t_{qe}(u)}{\partial u}\frac{du}{dt} = \frac{1}{2}T_q w, \tag{12}$$

$$w = \begin{bmatrix}\dot{\phi} & \dot{\theta} & \dot{\psi}\end{bmatrix}^T = \begin{bmatrix}w_x & w_y & w_z\end{bmatrix}^T, \tag{13}$$

$$T_q = \begin{bmatrix}-q_1 & -q_2 & -q_3 \\ q_0 & -q_3 & q_2 \\ q_3 & q_0 & -q_1 \\ -q_2 & q_1 & q_0\end{bmatrix}. \tag{14}$$

Therefore, the discretized state space representation in order to estimate the posture angles of the chisel are expressed by (15) and (16).

$$x_q(k) = x_q(k-1) + \Delta t \dot{q}(k), \tag{15}$$

$$y_q(k) = x_q(k) = \begin{bmatrix}q_0 & q_1 & q_2 & q_3\end{bmatrix}^T, \tag{16}$$

where k is the sampling number and Δt is the sampling period. In this study, we used extended Kalman filter[11] to estimate the state, which is quaternion since (15) is nonlinear as shown in Fig. 2. The system noise and observation noise needed to design the extended Kalman filter were given as $1.0 \times I_4$ and $0.21 \times I_4$, respectively, through preliminary experiments.

B. Measurement displacement of chisel

In this study, the IMU sensor and the LiDAR camera are used for estimating the displacement using sensor fusion technology. Fig. 4 shows the signal flow diagram of the chisel's displacement estimation proposed in the previous study[10]. The acceleration detected by the IMU sensor have the stationary biases such as gravitational acceleration. In the estimation of the chisel's displacement, drift is caused in the displacement by performing a double integral of the acceleration with the bias. In order to remove the biases, we apply the high-pass filter to the acceleration on each axis detected by IMU sensor. The high-pass filter can be performed as

$$a_{hpi}(k) = (1 - \Delta t w_h) a_{hpi}(k-1) + \Delta t a_i, \ (i = x, y, z), \tag{17}$$

where a_i, a_{hpi} are the acceleration before and after passing through the high-pass filter, respectively. The cut-off angular frequency was given as w_h = 100 rad/s through the preliminary experiments.

In addition, we used the LiDAR camera to estimate the displacement of the chisel more precisely. The LiDAR camera can detect color image and depth image. The chisel's location in the color image can be determined through object recognition using YOLO v4[12]. 1500 images with the chisel are used for the 2000 training in the chisel recognition. The loss rate of the chisel recognition is 0.35% in this approach. Therefore, it is enough to detect the chisel displacement.

The filtered acceleration through the high-pass filter and the displacement and velocity detected by the LiDAR camera are used in the steady-state Kalman filter. The discretized state space expressions in order to estimate the displacement and velocity are shown as

$$x_p(k) = A x_p(k-1) + B(k) a_{hp}(k), \tag{18}$$

$$y(k) = H x_p(k), \tag{19}$$

$$A = \begin{bmatrix} I_3 & O_{3\times3} & \Delta t I_3 \\ \Delta t I_3 & I_3 & O_{3\times3} \\ O_{3\times3} & O_{3\times3} & I_3 \end{bmatrix}, \tag{20}$$

$$B(k) = \begin{bmatrix} C(k) & O_{3\times3} & O_{3\times3} \end{bmatrix}^T, \tag{21}$$

$$x_p(k) = \begin{bmatrix} v(k) & p(k) & b_a(k) \end{bmatrix}^T, \tag{22}$$

$$H(k) = \begin{bmatrix} I_3 & O_{3\times3} & O_{3\times3} \\ O_{3\times3} & I_3 & O_{3\times3} \end{bmatrix}. \tag{23}$$

where $v(k)$, $p(k)$, $b_a(k)$ are the estimated velocity, displacement and the bias appeared in the acceleration, and $O_{3\times3}$ is 3-by-3 zero matrix. The observation vectors are displacement and velocity obtained from the LiDAR camera. The system noise of displacement and velocity were given as 0.5 and the bias appeared in the acceleration was given as 0.1. Observation noises were given as $0.1 \times I_4$ through preliminary experiments..

III. CHISELING AND SPLITTING MODEL

In the chiseling training simulator which is developed in our previous studies[8][9], the sensation of operation is driven by the admittance control system. This model is consist of the spring-mass-damper system with the moving equilibrium point as shown in Fig. 5.

The chiseling and splitting model proposed in this study is shown as

$$m_{vi}\ddot{p}_{vi}(t)+c_{vi}(\dot{p}_{vi}-\dot{p}_{di})+k_{vi}(p_{vi}-p_{di})=f_i,\ (i=x,y,z) \tag{24}$$

where p_{vi} is the position of the tip of the chisel in the virtual model, p_{di} is the equilibrium point, and f_i is the force applied by the operator. And m_{vi}, k_{vi}, and c_{vi} are the mass, spring constant, and viscosity coefficient of virtual model. Plastic deformation caused by the chiseling and splitting can be expressed by moving the equilibrium point. However, since the data due to force is impulsive, the equilibrium point velocity changes rapidly. Therefore, the low-pass filter is applied for suppressing the rapid changes in the equilibrium point motion. The continuous plastic deformation appeared in the experiment can be represented by the following model with the low-pass filter as

$$\begin{bmatrix}\dot{z}_l\\ \dot{p}_{di}\end{bmatrix}=\begin{bmatrix}-\frac{1}{T} & 0\\ 1 & 0\end{bmatrix}\begin{bmatrix}z_l\\ p_{di}\end{bmatrix}+\begin{bmatrix}\frac{1}{T}\\ 0\end{bmatrix}u, \tag{25}$$

$$\begin{bmatrix}\dot{p}_{di}\\ p_{di}\end{bmatrix}=\begin{bmatrix}1 & 0\\ 0 & 1\end{bmatrix}\begin{bmatrix}z_l\\ p_{di}\end{bmatrix}, \tag{26}$$

$$u(t)=\begin{cases}\alpha(f_i(t)-f_{dead}), & (f_i(t)>f_{dead})\\ 0, & (else)\end{cases} \tag{27}$$

where f_{dead}, T and α are the dead band of force, the time constant and scaling factor which amplifies the input difference f_i-f_{dead}. And z_l is the state variable of the low-pass filter. The impact of force on equilibrium point displacement is considered to vary between the initial chiseling of hard tissue and the subsequent splitting process. Therefore, the impulse in order to identify the chiseling and splitting operations is shown as

$$I_i(k)=\sum_{k=1}^{n} f_i(k)\Delta t,\ (i=x,y,z) \tag{28}$$

Each virtual parameter m_{vi}, c_{vi}, k_{vi}, α, and T was obtained through chiseling and splitting experiments conducted with the bone mallet on ABS resin. The parameters were adjusted to represent the experimental results in the model. The sensation of splitting hard tissues by the chisel under the chiseling force is represented by switching the virtual parameters and time constants from Table I(a) to (b). The model for switching the virtual parameters is represented by the equation (29).

$$[\alpha,T]=\begin{cases}\text{Model parameters (a) in Table I,}\\ (I_i(k)<I_{ib})\\ \text{Model parameters (b) in Table I,(else)}\end{cases} \tag{29}$$

IV. Experimental Verification

The effectiveness of the chiseling motion model was verified using chiseling motion measurement system. In this study, in order to obtain highly reproducible data, chiseling experiments were conducted on ABS resin printed with a 3D printer (FLASHFORGE Creator Pro, PPLE TREE). The ABS resin used in the experiment and its dimensions are shown in Fig. 6. The force was applied to the chisel with a vertical position to the z-axis. In addition, the dead band of force was given as $f_{dead}=-20$N, and the impulse of threshold value in order to split the ABS resin in the z-axis direction was given as $I_{zb}=3\times10^3$Ns through multiple experiments.

TABLE I

Parameters of virtual model on situations.

	Situation	m_{vi}, kg	c_{vi}, Ns/m	k_{vi}, N/m
(a)	Chiseling hard tissue	100	5×10^3	5×10^3
(b)	Chiseling though			

	T	α
(a)	0.7	4.0×10^{-3}
(b)	0.4	2.4×10^{-3}

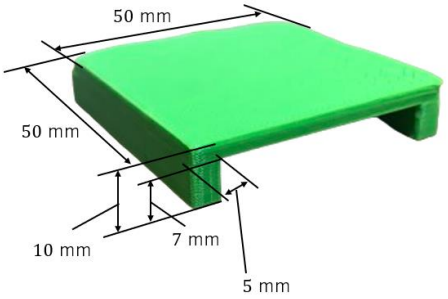

Fig. 6. ABS resin used in chiseling experiment.

V. Results and Discussion

In this study, chiseling force was applied twice to the ABS resin at 11.2 seconds and 15.8 seconds. The ABS resin was not split by the first chiseling force. But it was splitted due to the second chiseling force. Fig. 7 shows the results of the reaction force and reaction moment applied to the chisel, 7(a), 7(d), to 7(c) 7(f) are x to z- axis.

The results of translational motion detected by the LiDAR camera as shown in Fig. 8. Additionally, the measurement results of the displacement, velocity and posture and angular velocity of the chisel using sensor fusion are shown in Fig. Fig. 9 and Fig. 10 respectively. In Fig. 8, (a), (b), and (c) represent the displacements along the x, y, and z axes, respectively, and (d), (e), and (f) represent the velocities. Fig. 9 has same arrangement with Fig. 8. The displacement and velocity of the chisel detected by the LiDAR camera shown in Fig. 8 are used as observations of the Kalman filter in order to improve the accuracy. In Fig. 10, (a) and (b) represent the pitch angle, which is around the x axis and the yaw angle, which is around the y axis, respectively, and (c) and (d) represent the angular velocities. Fig. 9(c) shows that the chisel was displaced in the z-axis direction due to the chiseling force. The slight changes in the x and y axes

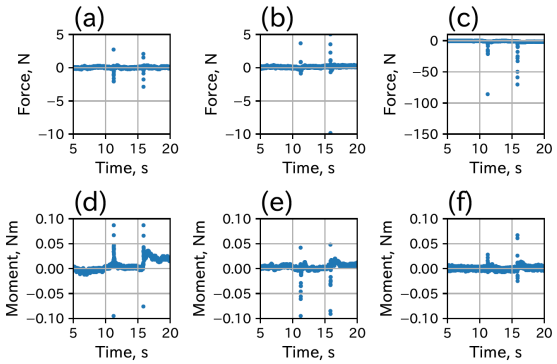

Fig. 7. Experimental results of operational force. (a) Change of x-axis reaction force; (b) Change of y-axis reaction force; (c) Change of z-axis reaction force; (d) Change of x-axis reaction moment; (e) Change of y-axis reaction moment; (f) Change of z-axis reaction moment.

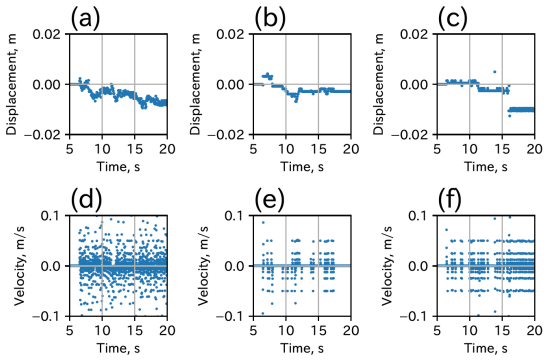

Fig. 8. Experimental results of chisel's displacement, velocity detected by LiDAR camera (a) Change of x-axis displacement; (b) Change of y-axis displacement; (c) Change of z-axis displacement; (d) Change of x-axis velocity; (e) Change of y-axis velocity; (f) Change of z-axis velocity.

shown in Fig. 9(a) and 9(b) are due to the changes in the yaw angle and pitch angle, respectively, and it can be confirmed from Fig. 10(a) and 10(b).

In this study, the displacement and velocity of the chisel in the chiseling model for the z-axis were adjusted to match the experimental measurements. The velocity and displacement of the equilibrium point change in the chiseling model for the z-axis are shown in Fig. 11(a) and Fig. 11(b), respectively. In addition, the comparison between the chiseling model and experimental results are shown in Fig. 12. Fig. 12(a) shows the comparison of the velocities, and (b) shows the comparison of the displacements. Fig. 12(b) shows that the chiseling model reflects the main characteristics of the measured chisel displacement. However, there are differences in the velocities, and the experimental results are delayed compared to the chiseling model results. This is because when the displacement and velocity of the chisel are corrected by the LiDAR camera, the velocity is derived from the backward difference of the displacement, resulting in a decrease in accuracy.

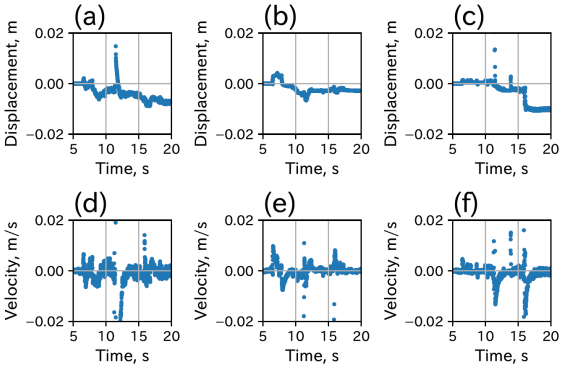

Fig. 9. Experimental results of chisel's displacement, velocity using sensor fusion. (a) Change of x-axis displacement; (b) Change of y-axis displacement; (c) Change of z-axis displacement; (d) Change of x-axis velocity; (e) Change of y-axis velocity; (f) Change of z-axis velocity.

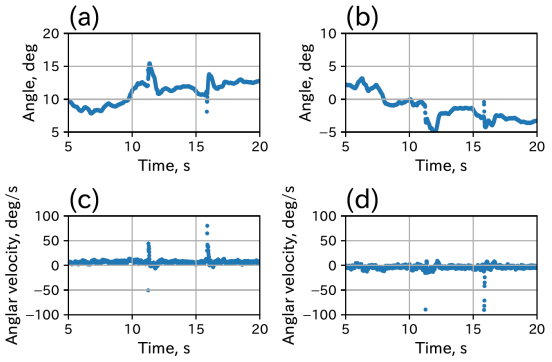

Fig. 10. Experimental results of chisel's angle, angular velocity using sensor fusion. (a) Change of pitch angle; (b) Change of yaw angle; (c) Change of pitch angular velocity; (d) Change of yaw angular velocity.

VI. CONCLUSIONS

In this study, the chiseling motion was represented as the spring-mass-damper system in which the displacement of the equilibrium point is varied. When the impulse of the striking force applied to the chisel exceeds the threshold, the model parameters of the equilibrium point displacement are switched, and the chiseling motion is expressed as the model. In addition, the effectiveness of the chiseling motion model was verified by conducting experiments using measurement system of chiseling motion. In the future works, we will improve the accuracy of the measurement system by integrating with optical cameras, such as motion capture. Furthermore, we will develop the model so that rotational and twisting movements can be represented virtually.

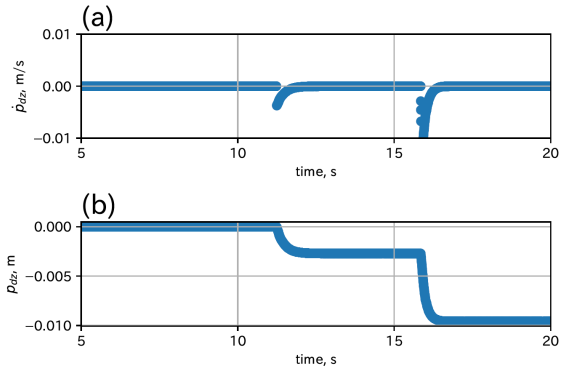

Fig. 11. Velocity and displacement of equilibrium point on the z-axis in chiseling. (a) Velocity of the equilibrium point; (b) Displacement of the equilibrium point.

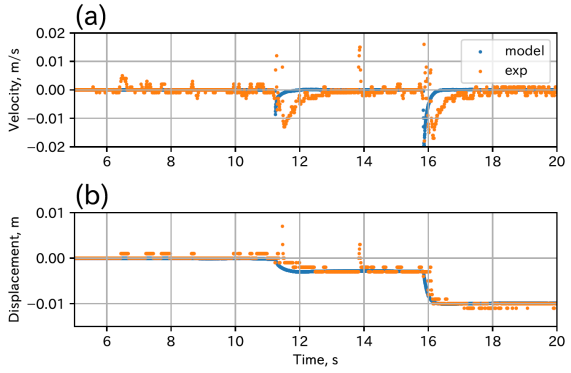

Fig. 12. Comparison of experimental results and chiseling model on z-axis. (a) Comparison of chisel's velocity on z-axis; (b) Comparison of chisel's displacement on z-axis.

REFERENCES

[1] Eugenia Yiannakopoulou, Nikolaos Nikiteas, Despina Perrea, et al., Virtual reality simulators and training in laparoscopic surgery, vol. 13, pp. 60-64, 2015

[2] Christina P. Rossitto ,Ian C. Odland, Holly Oemke, et al., External Ventricular Drain Training in Medical Students Improves Procedural Accuracy and Attitudes Toward Virtual Reality World Neurosurgery, vol. 175, pp.1246-1254, 2023.

[3] T Sohmura, H Hojo, M Nakajima, et al., Prototype of simulation of orthognathic surgery using a virtual reality haptic device, International Journal of Oral and Maxillofacial Surgery vol. 33, no. 8, pp. 740-750, 2004

[4] D. Escobar-Castillejos, J. Noguez, L. Neri, A. Magana, B. Benes, et al., A Review of Simulators with Haptic Devices for Medical Training, Journal of Medical Systems, vol. 40, no. 104, pp. 1-22, 2016

[5] Arikatla VS, Tyagi M, Enquobahrie A, et al,. High Fidelity Virtual Reality Orthognathic Surgery Simulator, Proccedings SPIE int Soc Opt Eng, 10576, 2018

[6] Lin Yanping, Wang Xudong, Development and validation of a surgical training simulator with haptic feedback for learning bone-sawing skill, Journal of Biomedical Informatics, vol. 48, pp. 122-129, 2014

[7] MING-SHIUM HSIEH, MING-DAR TSAI, et al., AN AMPUTATION SIMULATOR WITH BONE SAWING HAPTIC INTERACTION, Biomedical Engineering: Applications, Basis and Communications, vol. 18, No. 05, pp. 229-236, 2006

[8] Kentaro Masuyama, Yoshiyuki Noda, Yasumi Ito, et al., Instantaneous Reaction and Vibration Suppression Using Two-Degree-of-Freedom Admittance Control with H ∞ Feedback Controller in Surgical Training Simulator with Chiseling Operation, Journal of Robotics and Mechatronics, vol.34, no. 4, pp. 844-856, 2022.

[9] Masuyama K, Noda Y, Ito Y, Kagiyama Y, et al., Force display device and control system for surgical training simulator using bone chisel, In:IEEE International Conference on Biomedical Robotics and Biomechatronics, pp. 1248–1253, 2018.

[10] Shota Kasai, Sinyoung Lee, Yoshiyuki Noda, Development of measurement system of chiseling motion using sensor fusion technology, XXIV IMEKO World Congress, 2024

[11] Suzuki, S, K. Nonami, Navigation of Autonomous Drones in GPS and Non-GPS Space Using Extended Kalman Filter Measurement and Control, vol. 56, no. 9, 2017.

[12] Alexey Bochkovskiy, Chien-Yao Wang, Hong-Yuan Mark Liao, YOLOv4: Optimal Speed and Accuracy of Object Detection, arXiv preprint arXiv, pp. 1- 17,2020